Available online at www.sciencedirect.com
ScienceDirect
Comput. Methods Appl. Mech. Engrg. 335 (2018) 69–90
Computer methods in applied mechanics and engineering
www.elsevier.com/locate/cma

Stabilized mixed finite element method for the M_1 radiation model

Q. Schmid[a], Y. Mesri[a], E. Hachem[a,*], R. Codina[b]

[a] *MINES ParisTech, PSL - Research University, CEMEF - Centre de mise en forme des matériaux, CNRS UMR 7635, CS 10207 rue Claude Daunesse, 06904 Sophia Antipolis Cedex, France*
[b] *Universitat Politècnica de Catalunya, Jordi Girona 1-3, Edifici C1, 08034 Barcelona, Spain*

Received 25 August 2016; received in revised form 30 November 2017; accepted 26 January 2018
Available online 19 February 2018

Highlights

- New fully implicit mixed formulation for the M_1 radiative model.
- Implementing a new multidimensional stabilized finite element method for the M_1 model.
- Radiative transfer in a monolithic framework.
- First attempt to deal with coupled non-linear system that solves both radiative energy and radiative flux.

Abstract

In this work, we present a computational approach for the numerical simulation of thermal radiation. Radiation is modeled by solving a set of two coupled partial differential equations, the so-called M_1 model. A Variational Multiscale method is developed for this system, and tested on some illustrative benchmarks. The question of dealing with heterogeneous physical properties is also considered, and treated by means of an immersed method. It combines a level-set approach for representation of interfaces, mixing laws to build effective physical properties and an anisotropic mesh adaptation process, all these ingredients leading to an accurate description of the interface.

Keywords: Variational multiscale method; Stabilized finite elements; Radiation; Immersed volume method; Monolithic approach

1. Introduction

In many high temperature applications, such as industrial furnaces [1–3], glass treatment [4,5] nuclear engineering [6], or combustion and flame modeling [7–9], thermal radiation is the dominant mode of heat transfer. However, the full Radiative Transfer Equation (RTE), due to its seven variables dependency (three of space, two of directions, time and frequency) is, in many situation, too expensive to solve directly (particularly due to the angular dependency).

* Corresponding author.
E-mail addresses: Quentin.schmid@mines-paristech.fr (Q. Schmid), Youssef.mesri@mines-paristech.fr (Y. Mesri), Elie.Hachem@mines-paristech.fr (E. Hachem), ramon.codina@upc.edu (R. Codina).

https://doi.org/10.1016/j.cma.2018.01.046
0045-7825/

So, in recent years, with the growing power of computers, a great effort has been devoted to derive physically relevant models that are affordable from the numerical point of view (see [10], for instance).

The existing models differ in the way that angular dependency is treated. One of these models is for example the Spherical Harmonic approach, where the angular dependency of the specific intensity is expressed using Legendre polynomials [11]. Another class of methods is that based on direction-discretization approaches, in which the RTE is solved for a discrete set of directions, namely the discrete ordinates [12]; this leads to a system of ordinary partial differential equations, one for each discrete direction. However, in both cases, the price to pay to get a good numerical approximation is a high number of discrete ordinates or a high order Legendre polynomial, both of which come with a very high computational cost. There exist also other approaches, based on a totally different philosophy, like the "Surface-to-Surface" ($S2S$) or the zonal method [13]. The idea here is to compute net radiative exchanges between different parts of the computational domain (surface–surface, surface-volume and volume–volume exchanges). Then, those radiative exchanges are included in the global thermal balance. Within this framework, the radiation part is computed apart from the other physics in coupled problems (flow, heat transfer, turbulence). However, those approaches can become very computationally demanding for unsteady simulations, limiting the range of application of such methods.

In this paper we follow another approach, namely, the one based on moment models. In these models, the radiative transfer equation is averaged over all directions, which results in a classical coupled system of partial differential of a fixed number without angular dependency, but supplementary equations are needed to close the system. A well known closure is the P_1 model, but it has some well-identified drawbacks: it gives relevant results only when the absorption value is high and it cannot handle directional effects. A more sophisticated closure was proposed by Dubroca and Feugeas [14], who presented a hierarchy of models where the closure relationship is obtained through an under-constrained entropy maximization principle. This closure ensures desirable physical and mathematical properties. In this paper, the first member of this hierarchy, namely the M_1 radiation model, is used. Even if this model is relatively recent, it has been used by several teams, for radiation hydrodynamics [15,16], astrophysics applications [17,18] and also engineering situations where radiation interacts with fluid flow and heat transfer [19,20].

Furthermore, many situations require the possibility of representing different zones with different radiative properties (absorption coefficient mostly), or equivalently, a spatially dependent absorption; in this work, this is achieved by using an immersed volume method, which is based on the following ideas. First, the geometry of considered objects is represented using a signed distance function, like in [21]. Physical properties are calculated using an appropriate mixing law involving the distance function, so that different zones are treated in a monolithic way, with spatially-dependent physical properties. This approach is coupled to an anisotropic mesh adaptation technique [22], where the mesh is locally refined around the zero value of the level-set function, in order to represent accurately the geometry of considered objects and capture sharp gradients at the interface between zones. The numerical scheme that will be presented makes use of this way of modeling objects inside the enclosure.

For the M_1 model, as far as the authors are aware, all the numerical schemes are based on simplifying assumptions, like explicit treatments of some terms, and treating the system as a non-linear conservation law of a state vector. However, the system can also be viewed as a system of two coupled equations, so that a mixed formulation appears as an interesting lead. Here we use the terminology *mixed* formulation understanding that there are two different variables to approximate with different physical meaning and that could possibly be interpolated with different basis functions. Therefore, we intend here to design a fully implicit mixed formulation. It is known [23] that mixed formulations suffer from numerical oscillations when equal order interpolation is used for all variables. We propose to stabilize the formulation using the framework of the Variational Multiscale Method (VMS) [24,25], using the ideas that we have used in other examples that demonstrate the potential of the method, and that can be found in [26,21,27,28] . The main interest of this approach is the fact that it is general, in the sense that it offers a systematic way to stabilize a given discrete variational form. In this article we apply this idea to the M_1 model. To the best of the authors knowledge, this is the first attempt of such an approach for this problem.

Most of the numerical schemes for the M_1 are of Harten–Lax–van Leer (HLL) type [29], a finite volume method taking advantage of the hyperbolic eigenstructure of the system, which can be viewed as a non-linear conservation law. The work of Berthon and coworkers, that designed a series of "asymptotic preserving" schemes [30–32], can be quoted as an example. This work has been followed by an extension to radiation hydrodynamics, with the possibility of taking into account relativistic effects [33,34]. Two other approaches can also be cited, namely, one based on a

modified system of moments proposed in [35], and another one based on a discontinuous Galerkin approach credited to [36]. In both cases, applications remain restricted to one-dimensional situations. The goal of this paper is to propose and implement a new multidimensional mixed finite element method for the M_1 model. Moreover, some comparison with results of the P_1 model will be made, to highlight its limitations and show the discrepancies with the M_1 model.

This paper is organized as follows. In Section 2 we recall the basic equations of radiative transfer to derive the moment equations, and then we introduce the M_1 model. Section 3 recalls the tools used for multiphase computations. In Section 4 we will detail the weak formulation of the M_1 model that we propose. Section 5 is dedicated to the stabilization of the proposed formulation. In Section 6, we analyze the results of test cases to test the proposed formulation. Some concluding remarks close the paper in Section 7.

2. Governing equations of radiative transfer

2.1. The full radiative transfer equation

Let Ω be the computational domain and $\partial\Omega$ its boundary, assumed to be smooth enough. The considered time interval is $[0, T]$. A direction of the space $\boldsymbol{\omega}$ can be parametrized by two angles (φ, θ), so that we can write the direction vector as

$$\boldsymbol{\omega} = \begin{bmatrix} \cos(\theta)\sin(\varphi) \\ \sin(\theta)\sin(\varphi) \\ \cos(\varphi) \end{bmatrix}. \tag{1}$$

Let $\mathcal{S}$ denote the unit sphere. In what follows, the symbol $\int_{\mathcal{S}}$ means that the integration is performed over all the directions, i.e., for all $\boldsymbol{\omega} \in \mathcal{S}$, which is equivalent to say that $\varphi \in [0, 2\pi]$ and $\theta \in [0, \pi]$.

To ease the notation, the gray medium assumption is considered. This yields to equations integrated all over the frequency range, and therefore all the considered quantities will be frequency independent. The RTE permits to determine the specific radiative intensity $I(\boldsymbol{x}, t, \boldsymbol{\omega})$, which describes the density of photons at a given position, time and in a given direction. By considering an isotropic scattering to simplify the exposition, the full RTE reads:

$$\frac{1}{c}\frac{\partial I}{\partial t} + \boldsymbol{\omega}\cdot\nabla I = \frac{\sigma_r}{\pi}\kappa T^4 - (\kappa+\sigma)I + \frac{\sigma}{4\pi}\int_{\mathcal{S}} I(\boldsymbol{\omega}')d\omega'. \tag{2}$$

Here, $\kappa \geq 0$ is the absorption coefficient, $\sigma \geq 0$ the scattering coefficient, σ_r the Stephan–Boltzmann constant, c the light speed and T the (given) temperature field. An isotropic scattering is assumed here, but taking into account anisotropy could be done by introducing an appropriate diffusive angular distribution function in the integral of the last term, as done for example in [37].

As boundary condition, we prescribe I at inflows to a given function I^0, i.e.,

$$I(\boldsymbol{x}, t, \boldsymbol{\omega}) = I^0 \quad \text{for } \boldsymbol{x} \in \partial\Omega \text{ such that } \boldsymbol{\omega}\cdot\boldsymbol{n} < 0 \tag{3}$$

where $\boldsymbol{n}$ stands for the normal to the boundary, and I^0 can be related to the Planckian distribution. This type of boundary condition assumes that the boundary is black, that is to say, it absorbs all the incoming radiation (its emissivity ϵ equals one). However, this kind of boundary condition is a bit simplistic, and a more realistic boundary condition would be to consider a reflected part (related to the solution) and an emitted part (related to the Planck distribution), yielding

$$I(\boldsymbol{x}, t, \boldsymbol{\omega}) = \frac{(1-\varepsilon)}{\pi}\int_{\boldsymbol{\omega}\cdot\boldsymbol{n}<0} I(\boldsymbol{x}, t, \boldsymbol{\omega}')|\boldsymbol{\omega}'\cdot\boldsymbol{n}|d\boldsymbol{\omega}' + \frac{\varepsilon\sigma_r}{\pi}T_w^4 \quad \text{for } \boldsymbol{x} \in \partial\Omega \text{ such that } \boldsymbol{\omega}\cdot\boldsymbol{n} < 0. \tag{4}$$

On the one hand, (2) can be solved directly, using Monte-Carlo methods [38], but it is very computationally demanding, and it is prohibitive for 3D applications, in particular for unsteady resolutions. On the other hand, in many applications the quantity of interest is not the photon distribution itself but other macroscopic quantities, like mean energy or mean flux of the radiative field. This justifies the moment formulation that follows.

2.2. Moment models

Radiative energy E_r, radiative flux $\boldsymbol{F}_r$, and radiative pressure tensor $\mathbb{P}_r$, are defined as the zeroth,[1] first and second order angular moments of the specific radiative intensity, respectively, i.e.,

$$E_r = \int_{\mathcal{S}} I d\omega, \tag{5}$$

$$\boldsymbol{F}_r = \int_{\mathcal{S}} \boldsymbol{\omega} I d\omega, \tag{6}$$

$$\mathbb{P}_r = \int_{\mathcal{S}} (\boldsymbol{\omega} \otimes \boldsymbol{\omega}) I d\omega. \tag{7}$$

$\otimes$ being the dyadic product. Let us notice that (5) and (6) imply the two following so-called realizability conditions:

$$E_r \geq 0 \text{ since } I \geq 0, \tag{8}$$

and

$$\|\boldsymbol{F}_r\| \leq E_r \text{ since } \|\boldsymbol{\omega}\| = 1. \tag{9}$$

It can be shown (in [14] for example) that all couples $(E_r, \boldsymbol{F}_r)$ that fulfill those realizability conditions, namely the set of admissible states, defined by

$$\mathcal{C} = \{(E_r, \boldsymbol{F}_r) \in \mathbb{R} \times \mathbb{R}^d \text{ such } E_r \geq 0 \text{ and } \|\boldsymbol{F}_r\| \leq E_r\}, \tag{10}$$

is a closed convex cone. At this level, it is useful to define the reduced flux $\boldsymbol{f} = \frac{\boldsymbol{F}_r}{E_r}$ and $f = \|\boldsymbol{f}\|_2$ ($\|\|_2$ standing for the L^2 norm of a vector). The realizability conditions imply that $0 \leq f \leq 1$. We will see that, depending on the closure, those requirements are not necessarily fulfilled.

A general family of moment models is obtained by integrating (2) and multiplied by $\boldsymbol{\omega}$ over all $\mathcal{S}$, leading to

$$\frac{1}{c}\frac{\partial E_r}{\partial t} + \boldsymbol{\nabla} \cdot \boldsymbol{F}_r + \kappa E_r = 4\kappa\sigma_r T^4 \tag{11}$$

$$\frac{1}{c}\frac{\partial \boldsymbol{F}_r}{\partial t} + \boldsymbol{\nabla} \cdot \mathbb{P}_r + (\kappa + \sigma)\boldsymbol{F}_r = \boldsymbol{0}. \tag{12}$$

Here anisotropic scattering would require to introduce the moment of the phase function g, so that the last term of (12) would read $(\kappa + (1-g)\sigma)\boldsymbol{F}_r$ instead of $(\kappa + \sigma)\boldsymbol{F}_r$. Dealing with such a scattering term can be easily handled by the formulation that will be developed, since g is a constant.

This system needs supplementary equations to be closed, expressing $\mathbb{P}_r$ in terms of E_r and $\boldsymbol{F}_r$. Two closures are considered in this work. The first closure that will be investigated here is obtained using an under constraint maximization of a convex entropy functional [14], leading to the so-called M_1 model (more details can be found in [14,39,40]). This model reads:

$$\mathbb{P}_r = \underbrace{\left(\underbrace{\frac{1-\chi}{2}\mathbb{I}_d}_{=(1)} + \underbrace{\frac{3\chi - 1}{2}\frac{\boldsymbol{f} \otimes \boldsymbol{f}}{f^2}}_{=(2)} \right)}_{=\mathbb{D}(\boldsymbol{f}, f)} E_r, \tag{13}$$

$$\chi(f) = \frac{3 + 4f^2}{5 + 2\sqrt{4 - 3f^2}}. \tag{14}$$

We note that all the non-linearity of the M_1 model is in (13) and (14). Some comments about the physical insight of two contributions of the Eddington tensor can be given: term (1) can be viewed as an isotropic part of the radiative pressure, whereas term (2) is an anisotropic contribution in the direction of the normalized radiative flux $\boldsymbol{f}$. Those two terms are balanced by the Eddington factor $\chi(f)$, which is controlled by f, that can be viewed as a measure of the

[1] Sometimes the zeroth order moment is expressed omitting the factor $\frac{1}{c}$ and called the incident radiation G.

anisotropy of the radiation field. For example, one can see that for $f = 0$, corresponding to the diffusion limit, one gets

$$\chi(0) = \frac{1}{3}, \tag{15}$$

$$\mathbb{D}(\boldsymbol{f}, 0) = \frac{1}{3}\mathbb{I}_d. \tag{16}$$

For the transport limit, corresponding to $f = 1$, one obtains

$$\chi(1) = 1, \tag{17}$$

$$\mathbb{D}(\boldsymbol{f}, 1) = \frac{\boldsymbol{f} \otimes \boldsymbol{f}}{f^2}. \tag{18}$$

It shows that, thanks to the closure, both asymptotic regimes of radiative transfer, transport and diffusion, are satisfied by the M_1 model, contrary to model P_1.

To make comparisons, we will also consider the P_1 approximation, where the closure is obtained from (11) and (12) assuming an isotropic radiative pressure and a stationary radiative flux, leading to the following linear diffusion–reaction time dependent type equation (the radiative energy is usually denoted G in this context) :

$$\frac{1}{c}\frac{\partial G}{\partial t} - \boldsymbol{\nabla} \cdot \left(\frac{1}{3(\kappa + \sigma)}\boldsymbol{\nabla} G\right) + \kappa G = 4\sigma_r \kappa T^4. \tag{19}$$

Let us highlight that Eq. (19) corresponds to (11) in the diffusion limit.

Regarding the boundary conditions, it is not trivial to deduce relevant boundary conditions for the M_1 model similar to (3) and (4), since the radiative energy and fluxes are defined as angular averages of the radiative intensity, so they cannot be defined for a subset of $\mathcal{S}$. Indeed, this comes from the fact that the model was obtained through an angular averaging of the RTE. Nevertheless, in most of the cases [20,30], the following boundary conditions are used:

$$E_{r|\partial\Omega} = 4\pi\sigma_r T_w^4, \tag{20}$$

where T_w is the temperature of the considered wall. We also consider that no radiative flux is transmitted through the wall of the enclosure, which writes

$$\boldsymbol{F}_{r,|\partial\Omega} = \boldsymbol{0}. \tag{21}$$

The two boundary conditions (20) and (21) need to be compatible, since in principle any of these would produce a unique solution to the problem. An option to prescribe more realistic boundary conditions was proposed by Dubroca in a one dimensional case [41], and formalized by Frank et al. [42], with the concept of "partial" moments: other minimum entropy closure models can be derived by performing an averaging, not on the whole unit sphere $\mathcal{S}$, but on some subsets forming a partition of the unit sphere. For two dimensional problems the most straightforward is the "quarter" moment approximation, allowing to prescribe inflow radiation at different angles. However, the computational cost is extremely high, since one has to solve more equations (for a quarter moment model, four additional equations need to be solved) and on the other hand, the closure relation cannot be expressed analytically anymore.

3. Monolithic approach: immersed volume method

It is convenient here to give a quick summary of the immersed volume method and the anisotropic mesh adaptation technique used to deal with multi-domain problems.

3.1. Level-set approach

As mentioned before, the representation of a solid object can be done using a signed distance function. More formally, if $\Omega_{\text{solid}} \subset \Omega$ denotes the geometric domain occupied by the solid and Γ is its interface, the signed distance function $\alpha(\boldsymbol{x})$ is defined as

$$\alpha(\boldsymbol{x}) = \begin{cases} d(\boldsymbol{x}, \Gamma) \text{ if } \boldsymbol{x} \in \Omega_{\text{solid}} \\ -d(\boldsymbol{x}, \Gamma) \text{ if } \boldsymbol{x} \notin \Omega_{\text{solid}} \end{cases} \tag{22}$$

where $d(\boldsymbol{x}, \Gamma)$ is given by

$$d(\boldsymbol{x}, \Gamma) = \min_{\boldsymbol{y}\in\Gamma} \|\boldsymbol{x} - \boldsymbol{y}\|. \tag{23}$$

The distance function $\alpha(\boldsymbol{x})$ is now used to define a characteristic function of the solid domain, so that effective properties like $\kappa(\boldsymbol{x})$ in the domain can be expressed in terms of κ_{solid} and κ_{fluid} as follows:

$$\kappa(\boldsymbol{x}) = \kappa_{\text{solid}} H(\alpha(\boldsymbol{x})) + \kappa_{\text{fluid}}(1 - H(\alpha(\boldsymbol{x}))) \tag{24}$$

where $H(\alpha)$ is a smoothed Heaviside function, as proposed in [21].

3.2. Anisotropic mesh adaptation

The level-set approach exposed above has to be coupled with an anisotropic mesh adaptation technique to assign the thermodynamical properties on the both sides of the interface. This technique relies on building an edge-based a priori error estimation, used to construct a metric field that measures an interpolation error along each edge and in the direction of each edge. The metric field is a second order positive tensor, and thus we can derive an inner product and an associated norm, so that an ideal element has a unit area with respect to this norm. This error estimation is then used to compute stretching factors, and the mesh is modified based on a conformity control through a minimal volume theorem. More details can be found in [22] and [43].

4. Mixed finite element formulation for the M_1 radiation model

4.1. Weak formulation

We now turn to the weak formulation for the M_1 model, defined by Eqs. (11), (12), (13) and (14). Let Q be the space where E_r belongs for each time t and W the space where $\boldsymbol{F}_r$ belongs, i.e., $E_r(\cdot, t) \in Q$, $\boldsymbol{F}_r(\cdot, t) \in W$ for all $t > 0$. The spaces for the test functions will be denoted by Q_0 and W_0, so that functions in these spaces will be zero where functions in the corresponding trial spaces will be prescribed with Dirichlet boundary conditions. To avoid technical details, appropriate regularity in both space and time will be assumed.

For conciseness, let us consider as boundary conditions that the normal component of $\mathbb{P}_r$ (which yields a prescription for E_r) or the normal component of $\boldsymbol{F}_r$ are prescribed on the boundary, the former weakly and the latter strongly. These could be changed by modifying the functional setting of the problem. To simplify the exposition, when E_r is prescribed we assume that it is to zero. The weak formulation of the problem is now obtained by multiplying (11) by $q \in Q_0$ and (12) by $\boldsymbol{w} \in W_0$, integrating over the computational domain and using integration by parts on the term involving $\mathbb{P}_r$. This leads to the following problem:

Find $(\boldsymbol{F}_r, E_r) \in W \times Q$ such that for all $(\boldsymbol{w}, q) \in W_0 \times Q_0$

$$\frac{1}{c}\left\langle \frac{\partial \boldsymbol{F}_r}{\partial t}, \boldsymbol{w} \right\rangle + \langle(\kappa + \sigma)\boldsymbol{F}_r, \boldsymbol{w}\rangle - \langle \mathbb{P}_r, \nabla \boldsymbol{w}\rangle = 0, \tag{25}$$

$$\frac{1}{c}\left\langle \frac{\partial E_r}{\partial t}, q \right\rangle + \langle \kappa E_r, q\rangle + \langle \nabla \cdot \boldsymbol{F}_r, q\rangle = \langle 4\kappa\sigma_r T^4, q\rangle. \tag{26}$$

Here and in the following, $\langle f, g\rangle = \int_\Omega fg$ for any functions f and g, vector or scalar valued.

4.2. Time discretization and treatment of the non-linear term

Let us consider a uniform partition of the time interval $[0, T]$, so that $0 = t^0 < t^1 < \cdots < t^N = T$, with $\delta t := t^{n+1} - t^n$ constant, $n = 0, \ldots, N-1$. The time discretization will be performed using standard finite difference schemes. Using for example backward differences, for a generic time dependent function $g(t)$, the time derivative at t^n can be approximated by an appropriate incremental quotient $\frac{\delta g^n}{\delta t}$, with δg^n depending on g^{n-k}, $k = 0, 1, \ldots$, and g^n being an approximation to $g(t^n)$. In particular, in the numerical examples we will use the simplest backward Euler scheme, in which $\delta g^n = g^n - g^{n-1}$ and all terms in the equation are evaluated at t^n. Since there is no possibility of confusion, the superscript with the time step level will be omitted.

As mentioned in Section 1, all the non-linearity of the M_1 model is contained in $\mathbb{P}_r$. Hence, this term has to be treated in an appropriate manner, by performing non-linear iterations within each time step. Introducing a superscript counter i for these iterations, we can consider the following expansion of the radiative pressure tensor:

$$\mathbb{P}_r^{i+1} \approx \mathbb{P}_r^i + \mathbb{J}_E^i(E_r^{i+1} - Er^i) + \underline{\mathbb{J}_F^i}(\boldsymbol{F}_r^{i+1} - \boldsymbol{F}_r^i) \tag{27}$$

where $\mathbb{J}_E^i$ and $\underline{\mathbb{J}_F^i}$[2] are the Jacobian matrixes of $\mathbb{P}_r$ with respect to E_r and $\boldsymbol{F}_r$, respectively. The calculation of those matrixes is detailed in the Appendix. Introducing (27) into (25) and (26), one gets

$$\begin{aligned}
&\frac{1}{c}\left\langle \frac{\delta \boldsymbol{F}_r^{i+1}}{\delta t}, \boldsymbol{w} \right\rangle + \langle(\kappa+\sigma)\boldsymbol{F}_r^{i+1}, \boldsymbol{w}\rangle - \langle \underline{\mathbb{J}_F^i}\,\boldsymbol{F}_r^{i+1}, \boldsymbol{\nabla w}\rangle - \langle \mathbb{J}_E^i E_r^{i+1}, \boldsymbol{\nabla w}\rangle \\
&\qquad = \langle \mathbb{P}_r^i, \boldsymbol{\nabla w}\rangle - \langle \underline{\mathbb{J}_F^i}\,\boldsymbol{F}_r^i, \boldsymbol{\nabla w}\rangle - \langle \mathbb{J}_E^i E_r^i, \boldsymbol{\nabla w}\rangle,
\end{aligned} \tag{28}$$

$$\frac{1}{c}\left\langle \frac{\delta E_r^{i+1}}{\delta t}, q \right\rangle + \langle \kappa E_r^{i+1}, q\rangle + \langle \boldsymbol{\nabla}\cdot\boldsymbol{F}_r^{i+1}, q\rangle = \langle 4\kappa\sigma_r T^4, q\rangle. \tag{29}$$

This is a classical Newton–Raphson iteration procedure within each time step, but other options could be implemented. Further investigation about linearization and convergence issues has to be conducted, and will be addressed in a forthcoming paper (see [26] for more details).

4.3. Galerkin finite element approximation

Let us consider a finite element partition $\mathcal{T}_h = \{K\}$ of the computational domain of diameter h. From this we may construct finite element spaces $W_h \subset W$, $W_{h,0} \subset W_0$, $Q_h \subset Q$ and $Q_{h,0} \subset Q_0$ in the usual way. Finite element functions will be identified with a subscript h.

The Galerkin finite element approximation to problem (28)–(29) reads: for each iteration $i+1$ of each time step, find $\boldsymbol{F}_{r,h}^{i+1} \in W_h$, $E_{r,h}^{i+1} \in Q_h$ such that

$$\begin{aligned}
&\frac{1}{c}\left\langle \frac{\delta \boldsymbol{F}_{r,h}^{i+1}}{\delta t}, \boldsymbol{w}_h \right\rangle + \langle(\kappa+\sigma)\boldsymbol{F}_{r,h}^{i+1}, \boldsymbol{w}_h\rangle - \langle \underline{\mathbb{J}_F^i}\,\boldsymbol{F}_{r,h}^{i+1}, \boldsymbol{\nabla w}_h\rangle - \langle \mathbb{J}_E^i E_{r,h}^{i+1}, \boldsymbol{\nabla w}_h\rangle \\
&\qquad = \langle \mathbb{P}_r^i, \boldsymbol{\nabla w}_h\rangle - \langle \underline{\mathbb{J}_F^i}\,\boldsymbol{F}_{r,h}^i, \boldsymbol{\nabla w}_h\rangle - \langle \mathbb{J}_E^i E_{r,h}^i, \boldsymbol{\nabla w}_h\rangle,
\end{aligned} \tag{30}$$

$$\frac{1}{c}\left\langle \frac{\delta E_{r,h}^{i+1}}{\delta t}, q_h \right\rangle + \langle \kappa E_{r,h}^{i+1}, q_h\rangle + \langle \boldsymbol{\nabla}\cdot\boldsymbol{F}_{r,h}^{i+1}, q_h\rangle = \langle 4\kappa\sigma_r T^4, q_h\rangle, \tag{31}$$

for all $\boldsymbol{w}_h \in W_{h,0}$ and $q_h \in Q_{h,0}$. It is understood that the Jacobians and the pressure radiation tensor are computed with the finite element unknowns.

This is the classical Galerkin finite element method for the M_1 radiation model. To the best of the authors knowledge, there is no other finite element method available in the literature for this model.

5. Stabilization for the proposed formulation

It was observed that the solution of the proposed formulation (30)–(31) suffers from numerical oscillations when it is used in the way we presented it above, with linear finite element interpolation for all the unknowns. The reason for this is that the problem we are solving is a highly nonlinear wave equation written in mixed form, and therefore there is a need to satisfy an inf–sup condition between the unknowns. To explain the situation, we may consider the linear problem that is obtained if in (11)–(12) we take $\kappa = 0$, $\sigma = 0$ and take $f = 0$ (diffusive limit) in $\mathbb{P}_r$. Then we get

$$\begin{aligned}
&\frac{1}{c}\frac{\partial E_r}{\partial t} + \boldsymbol{\nabla}\cdot\boldsymbol{F}_r = 0, \\
&\frac{1}{c}\frac{\partial \boldsymbol{F}_r}{\partial t} + \frac{1}{3}\boldsymbol{\nabla} E_r = \boldsymbol{0},
\end{aligned}$$

[2] Let us note that $\underline{\mathbb{J}_F^i}$ is a third order tensor, see Appendix A.1.

which is the classical wave equation written in mixed form, and which needs to be supplemented with boundary conditions and initial conditions that will drive the solution. In the nonlinear problem, the functional setting where the solution is well posed is not known, to our knowledge. However, the mathematical structure of the linear wave equation is well understood. The possible variational problems associated to it are described in detail in [44] (see also [45] for the analysis of the time discretization schemes and [46] for the application of the Sommerfeld boundary condition to this problem). For each time t, we may choose for example $\boldsymbol{F}_r$ to belong to $H(\mathrm{div},\,\Omega)$ (vector functions in $L^2(\Omega)^d$ with divergence in $L^2(\Omega)$) and E_r to belong to $L^2(\Omega)$. In any case, the functional spaces in play satisfy an inf–sup condition that is not inherited at the discrete level, in particular when using equal interpolation for all the unknowns, and therefore oscillations may appear. The problem we are dealing with is much more complex, but of course the difficulties of the underlying linear problem will remain. We have observed the oscillations mentioned in practice, particularly in the field E_r.

To circumvent the issue, we propose to stabilize the formulation using the VMS framework, like done in [47] for the Navier–Stokes equations, or in [48,44] for the wave equation in mixed form.

5.1. Scale splitting within the VMS framework

Once the equations to be solved are written in variational form, a VMS decomposition is applied and the radiative flux and energy are split into a coarse-scale/fine-scale decomposition, and likewise for the associated test functions. Thus, the corresponding spaces can be written as $W = W_h \oplus W'$ and $Q = Q_h \oplus Q'$, and the functions belonging to them as

$$\begin{aligned}
&\boldsymbol{F}_r = \boldsymbol{F}_{r,h} + \boldsymbol{F}'_r, \quad E_r = E_{r,h} + E'_r,\\
&\boldsymbol{w} = \boldsymbol{w}_h + \boldsymbol{w}', \quad q = q_h + q',
\end{aligned}$$

where $\boldsymbol{w}$ will be the test function for $\boldsymbol{F}_r$ and q the test function for E_r, the subscript h refers to the finite element component and the prime to the subgrid scale component.

At each iteration we have to solve a linear problem. For sake of clarity, the following notations are introduced:

$$\mathbb{F}_f = \mathbb{P}^i_r - \underline{\mathbb{J}^i_F}\,\boldsymbol{F}^i_{r,h} - \mathbb{J}^i_E E^i_{r,h}, \tag{32}$$

$$f_E = 4\kappa\sigma_r T^4. \tag{33}$$

Note that, for the converged solution, the last two terms in (32) will cancel with $-\underline{\mathbb{J}^i_F}\,\boldsymbol{F}^{i+1}_{r,h} - \mathbb{J}^i_E E^{i+1}_{r,h}$ in the left-hand-side. However, we have kept the latter in the differential operator for generality. The finite element residuals to be introduced later, on which the stabilized formulation depends, will not contain these terms in the converged solution.

Since there is no possibility of confusion, superscripts denoting the iteration counter are omitted in the following. Introducing the previous decompositions into the weak formulation leads to a coarse-scale and a fine scale problem for each unknown, which read:

- Radiative flux equation

$$\begin{aligned}
&\frac{1}{c}\left\langle\frac{\delta(\boldsymbol{F}_{r,h}+\boldsymbol{F}'_r)}{\delta t},\boldsymbol{w}_h\right\rangle + \langle(\kappa+\sigma)(\boldsymbol{F}_{r,h}+\boldsymbol{F}'_r),\boldsymbol{w}_h\rangle - \langle\underline{\mathbb{J}_F}\,(\boldsymbol{F}_{r,h}+\boldsymbol{F}'_r),\nabla\boldsymbol{w}_h\rangle\\
&\qquad - \langle\mathbb{J}_E(E_{r,h}+E'_r),\nabla\boldsymbol{w}_h\rangle = \langle\mathbb{F}_f,\nabla\boldsymbol{w}_h\rangle,
\end{aligned} \tag{34}$$

$$\begin{aligned}
&\frac{1}{c}\left\langle\frac{\delta(\boldsymbol{F}_{r,h}+\boldsymbol{F}'_r)}{\delta t},\boldsymbol{w}'\right\rangle + \langle(\kappa+\sigma)(\boldsymbol{F}_{r,h}+\boldsymbol{F}'_r),\boldsymbol{w}'\rangle - \langle\underline{\mathbb{J}_F}\,(\boldsymbol{F}_{r,h}+\boldsymbol{F}'_r),\nabla\boldsymbol{w}'\rangle\\
&\qquad - \langle\mathbb{J}_E(E_{r,h}+E'_r),\nabla\boldsymbol{w}'\rangle = \langle\mathbb{F}_f,\nabla\boldsymbol{w}'\rangle.
\end{aligned} \tag{35}$$

- Radiative energy equation

$$\frac{1}{c}\left\langle\frac{\delta(E_{r,h}+E'_r)}{\delta t},q_h\right\rangle + \langle\nabla\cdot(\boldsymbol{F}_{r,h}+\boldsymbol{F}'_r),q_h\rangle + \langle\kappa(E_{r,h}+E'_r),q_h\rangle = \langle f_E,q_h\rangle, \tag{36}$$

$$\frac{1}{c}\left\langle\frac{\delta(E_{r,h}+E'_r)}{\delta t},q'\right\rangle + \langle\nabla\cdot(\boldsymbol{F}_{r,h}+\boldsymbol{F}'_r),q'\rangle + \langle\kappa(E_{r,h}+E'_r),q'\rangle = \langle f_E,q'\rangle. \tag{37}$$

5.2. Approximation for the fine-scale problem

At this point, the efficiency of the stabilization will rely on the way that the fine scales $\boldsymbol{F}'_r$ and E'_r are modeled. For this calculation, the following assumptions are considered:

- It is a classical assumption to consider subscales that vanish on element boundaries. See [49] for a way to generalize this.
- "Quasi-static" subscales are considered, in the sense that we do not track their evolution in time. This assumption is made in many cases. However, these fine-scales are not time-independent, since they are driven by large-scale time-dependent residuals.
- Even though all the non-linear terms involving the Jacobian matrixes $\mathbb{J}_E$ and $\underline{\mathbb{J}_F}$ depend in principle on $\boldsymbol{F}'_r$ and E'_r, this dependency will be neglected, i.e., non-linear terms will be approximated using only the large-scale components.
- It should be noted that the final stabilized formulation will depend on the linearization chosen. In general, for nonlinear problems one can follow two possible equivalent paths. In the first, one could design a stabilization method for the nonlinear problem, then linearize it and then approximate the subscales. In the second, one can linearize first the problem and then approximate the subscales (this is what we have done). Whichever the problem for the subscales is, it will be approximated, replacing the differential operator involved by a matrix of stabilization parameters. This approximation depends of course on the operator chosen, and each choice will lead to a different stabilization method (see [50], Section 4.3.1).
- We will make use of the algebraic subgrid scale (ASGS) formulation, as defined in [51] and described below.

Let us introduce the following notation:

$$\mathfrak{R}_{\boldsymbol{F},\mathbf{1}} = -(\kappa+\sigma)\,\boldsymbol{F}_{r,h} - \frac{1}{c}\frac{\delta \boldsymbol{F}_{r,h}}{\delta t}, \tag{38}$$

$$\mathbb{R}_{F,2} = \mathbb{F}_f + \underline{\mathbb{J}_F}\,\boldsymbol{F}_{r,h} + \mathbb{J}_E E_{r,h}, \tag{39}$$

$$\mathfrak{R}_E = f_E - \frac{1}{c}\frac{\delta E_{r,h}}{\delta t} - \boldsymbol{\nabla}\cdot\boldsymbol{F}_{r,h} - \kappa E_{r,h}, \tag{40}$$

$$\mathbb{A} = \mathbb{J}_{\boldsymbol{F}}\,\boldsymbol{F}'_r + \mathbb{J}_E E'_r. \tag{41}$$

With the assumptions described above, the fine scale problem (35)–(37) then reads:

$$\langle(\kappa+\sigma)\boldsymbol{F}'_r, \boldsymbol{w}'\rangle - \langle\mathbb{A}, \boldsymbol{\nabla}\boldsymbol{w}'\rangle = \langle\mathfrak{R}_{\boldsymbol{F},\mathbf{1}}, \boldsymbol{w}'\rangle + \langle\mathbb{R}_{F,2}, \boldsymbol{\nabla}\boldsymbol{w}'\rangle, \tag{42}$$

$$\langle\boldsymbol{\nabla}\cdot\boldsymbol{F}'_r, q'\rangle + \langle\kappa E'_r, q'\rangle = \langle\mathfrak{R}_E, q'\rangle. \tag{43}$$

At this point, let us recall that the fine scale problem does not really need to be solved in a precise way, it just has to be approximated in order to capture the effect of the fine scales on the large scales.

Since the fine scales vanish on inter-element boundaries, we can write

$$\langle\mathbb{A}, \boldsymbol{\nabla}\boldsymbol{w}'\rangle = -\langle\boldsymbol{\nabla}\cdot\mathbb{A}, \boldsymbol{w}'\rangle,$$
$$\langle\mathbb{R}_{F,2}, \boldsymbol{\nabla}\boldsymbol{w}'\rangle = -\langle\boldsymbol{\nabla}\cdot\mathbb{R}_{F,2}, \boldsymbol{w}'\rangle.$$

We can now define

$$\mathfrak{R}_{\boldsymbol{F}} = \mathfrak{R}_{\boldsymbol{F},\mathbf{1}} - \boldsymbol{\nabla}\cdot\mathbb{R}_{F,2}.$$

The term $\boldsymbol{\nabla}\cdot\mathbb{A}$ requires to make more assumptions. Since only the steady state is of interest, spatial variations of the Jacobian matrixes in the left-hand side can be neglected without compromising the accuracy of the scheme. Hence, by denoting $\underline{\mathbb{J}_F} = (\mathbb{J}^p_F)_{p\in\{1,\dots,d\}}$, we can write

$$\boldsymbol{\nabla}\cdot\mathbb{A} = \mathbb{J}_E\boldsymbol{\nabla}E'_r + \sum_{p=1}^{d}\mathbb{J}^p_F\boldsymbol{\nabla}F'_{r,p}. \tag{44}$$

Using this, the fine-scale problem can be written as

$$\langle(\kappa+\sigma)\boldsymbol{F}'_r + \mathbb{J}_E\nabla E'_r + \sum_{p=1}^{d}\mathbb{J}_F^p\nabla F'_{r,p}, \boldsymbol{w}'\rangle = \langle\mathfrak{R}_{\boldsymbol{F}}, \boldsymbol{w}'\rangle, \tag{45}$$

$$\langle\nabla\cdot\boldsymbol{F}'_r + \kappa E'_r, q'\rangle = \langle\mathfrak{R}_E, q'\rangle \tag{46}$$

for all test functions $\boldsymbol{w}'$ and q'. This problem can be cast in the following abstract form

$$P'(\mathcal{L}(\boldsymbol{U})) = P'(\mathfrak{R}), \tag{47}$$

with

$$\boldsymbol{U} = \begin{bmatrix}\boldsymbol{F}'_r\\ E'_r\end{bmatrix}, \qquad \mathfrak{R} = \begin{bmatrix}\mathfrak{R}_{\boldsymbol{F}}\\ \mathfrak{R}_E\end{bmatrix}.$$

$\mathcal{L}$ is the differential operator appearing in the left-hand-side of (45)–(46) and P' is the projection onto the space of subscales. In essence, the two common choices for this operator are to take it either the projection orthogonal to the finite element space (OSS method) or the identity when applied to finite element residuals (ASGS method); see [47]. As mentioned before, the ASGS formulation will be used in this work.

The idea is now to approximate the operator $\mathcal{L}$ by an operator easy to invert. A straightforward solution is to take $\mathcal{L}^{-1}\approx\mathbb{T}$, where $\mathbb{T}$ is a diagonal matrix. Thus, we take

$$\mathbb{T} = \begin{bmatrix}\tau_F\mathbb{I}_d & 0\\ 0 & \tau_E\end{bmatrix}.$$

We want to avoid the use of bubble functions for the choice of stabilization parameters, so we will follow the approach proposed in [47]. This is achieved through an analysis using the Fourier transform with respect to the space coordinate $\boldsymbol{x}$, and imposing $\mathbb{T}$ to be close to $\mathcal{L}^{-1}$ in a spectral sense. Let us consider the Fourier transform of a generic function U as

$$\widehat{U}(\boldsymbol{k}) = \int_K U(\boldsymbol{x})\exp\Big(-\frac{\mathrm{i}\boldsymbol{k}\cdot\boldsymbol{x}}{h}\Big)dK,$$

where $\mathrm{i}=\sqrt{-1}$ and K is an element of the finite element partition. Applying this transform to (47) gives:

$$(\kappa+\sigma)\widehat{\boldsymbol{F}'_r} - \mathbb{J}_E\frac{i\boldsymbol{k}}{h}\widehat{E'_r} - \sum_{p=1}^{d}\mathbb{J}_F^p\frac{i\boldsymbol{k}}{h}\widehat{F'_{r,p}} = \widehat{\mathfrak{R}_{\boldsymbol{F}}}, \tag{48}$$

$$-\frac{i\boldsymbol{k}}{h}\cdot\widehat{\boldsymbol{F}'_r} + \kappa\widehat{E'_r} = \widehat{\mathfrak{R}_E}, \tag{49}$$

where we have assumed again that subscales vanish on the element boundaries.

At this stage, we would like to point out that the governing equations of the M_1 model are similar to a system of damped waves in mixed form, like that addressed in [52]. This leads us to make an analogy with the approach proposed in [48,53] or [54,46,45] for undamped waves, and choose the stabilization parameters as

$$\tau_F = \frac{1}{\sqrt{\left(\frac{c_1(\rho(\mathbb{J}_E)+\sum_{i=1}^{d}\rho(\mathbb{J}_F^i))}{h}\right)^2 + (\kappa+\sigma)^2}}, \tag{50}$$

$$\tau_E = \frac{1}{\sqrt{(\frac{c_2}{h})^2+\kappa^2}}, \tag{51}$$

where $\rho(\cdot)$ stands for the spectral radius of a matrix and c_1 and c_2 are algorithmic constants, whose values are $c_1=2.0$ and $c_2=4.0$ (see [47] for further discussion about these constants). We finally get

$$\boldsymbol{F}'_r = \tau_F\mathfrak{R}_{\boldsymbol{F}}, \quad E'_r = \tau_E\mathfrak{R}_E. \tag{52}$$

Then, one just need to introduce (52) in (34) and (36) after integrating by parts the terms involving the subscales, leading to new terms in the previous formulation that provide the desired extra control. The stabilization mechanisms introduced by the subscales are the same as for the linear wave equation in mixed form; see [48,44].

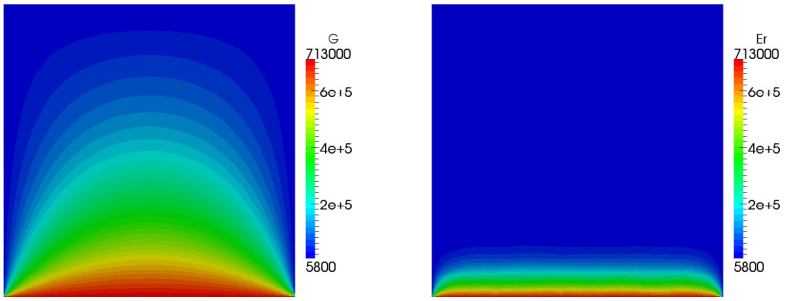

Fig. 1. Radiative energy for P_1 model (left) and M_1 model (right): $t = 5\delta t$.

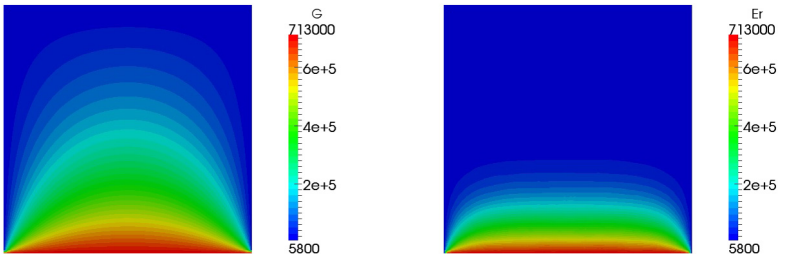

Fig. 2. Radiative energy for P_1 model (left) and M_1 model (right): $t = 25\delta t$.

6. Numerical results

This section is devoted to the testing of the formulation on four benchmark problems available in the literature, in order to assess the implementation of the new mixed stabilized finite element method. The first example considers one single domain, whereas the three other problems deal with multidomains to illustrate the use of the immersed-volume method for such situations.

In all what follows, we make use of unstructured meshes of triangular linear elements. A classical backward Euler scheme is used for the time discretization, and the spatial discretization is performed using linear P_1 elements. For linear system resolutions, a BiCGSTAB solver is used for all computations, preconditioned with an incomplete LU factorization. Regarding the behavior of the non-linear scheme, it is worth mentioning that for the three last cases examples involving the use of the immersed volume method, the non linear solver took more iteration to converge that for the first case. The tolerance for the convergence of the linear solver, usually set to 10^{-6} in our library, was slightly relaxed (up to $5.5\,10^{-5}$).

6.1. Transparent media in a square enclosure

For our first example, we consider radiative transfer in a static non-participating media contained in the unit square. This test case is close to the ones presented in [55] and [37] or [20], with the difference that we set here $\kappa = 0\ \mathrm{m}^{-1}$. We want to make a comparison with the P_1 model, so we also perform the computation with $\kappa = 10^{-4}\ \mathrm{m}^{-1}$ and $c = 1$. We use Dirichlet boundary conditions with a bottom wall at a fixed $E_{r,in} = 7.13\ 10^5$ W and the other walls are at $E_{r,b} = 5800$ W, and a zero value is fixed for the normal component of $\boldsymbol{F}_r$. Note that for the continuous problem we can prescribe either E_r or the normal component of $\boldsymbol{F}_r$, but in principle not both. However, for the discrete problem this is possible as soon as both prescriptions yield the same approximation. A similar strategy is used for example in [20]; see also the discussion at the end of Section 2. The initial radiative energy is $E_{r,0} = 5800$ W. For both simulations, the time step is $\delta t = 0.05$, and we use a mesh of approximately 11 200 elements.

First, the obtained radiative distribution in Figs. 1–4 are in agreement with [37]. The results also show the ability of the M_1 model to reproduce the transient behavior of the phenomenon represented. Indeed, it is observed that for the P_1 model, the equilibrium state is reached after only one time step, and using a smaller time step does not

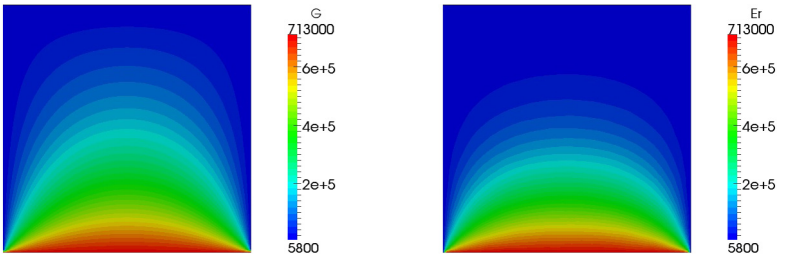

Fig. 3. Radiative energy for P_1 model (left) and M_1 model (right): $t = 400\delta t$.

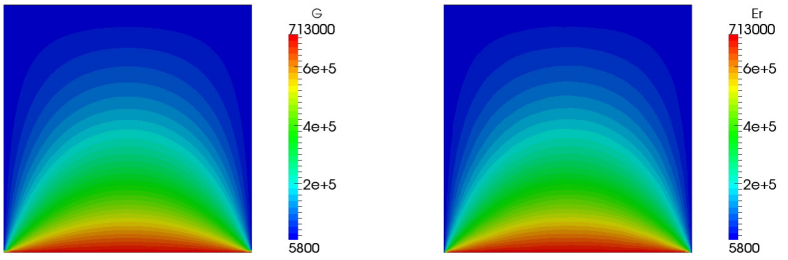

Fig. 4. Radiative energy for P_1 model (left) and M_1 model (right): steady state.

make any difference. However, even if the P_1 model is not able to reproduce the unsteady evolution, the final state obtained by the two models is the same. Hence, one could argue that, since the transient part is occurring at very fast time scales (because of the magnitude of c) compared to the characteristic times of other physical phenomena (heat transfer, flow, etc.) with which the radiation is coupled, only the steady state is important. This example demonstrates that the obtained solution is free of oscillations, justifying the coupled formulation and the stabilization developed here.

6.2. *Participating media with discontinuous coefficients: fixed temperature*

This case is taken from [56], where solutions of different approximate models for radiation ($\mathbb{P}_1$, simplified $\mathbb{P}_n$ approximations [57], partial-space entropy moment approximation [42]) are compared to solutions obtained by a direct resolution of Eq. (2), so it offers a reference to compare our results. We considered a fixed temperature, constant in two different subdomains, with a spatially dependent absorption coefficient κ. The computational domain is $\mathcal{D} = [0, 1] \times [0, 10]$, and we define $\mathcal{D}_0 = [0.45, 0.55] \times [4.5, 5.5]$, $\mathcal{D}_1 = \mathcal{D} \setminus \mathcal{D}_0$. We set $\sigma = 1$ and the temperature and absorption coefficients are taken as

$$T(\boldsymbol{x}) = \begin{cases} 1000 \text{ K} & \text{if } \boldsymbol{x} \in \mathcal{D}_0 \\ 1800 \text{ K} & \text{if } \boldsymbol{x} \in \mathcal{D}_1, \end{cases} \tag{53}$$

$$\kappa(\boldsymbol{x}) = \begin{cases} 3 \text{ m}^{-1} & \text{if } \boldsymbol{x} \in \mathcal{D}_0 \\ 1 \text{ m}^{-1} & \text{if } \boldsymbol{x} \in \mathcal{D}_1. \end{cases} \tag{54}$$

This temperature leads to a "manufactured" source term for Eq. (11), varying is space, but constant in time. The Immersed Volume Method allows us to represent the spatial dependence of the absorption coefficient in a natural way.

The mesh used for the computations and the representation of the level-set function of the object are displayed in Fig. 5; this mesh is composed of 218 072 elements. We use a zero Dirichlet condition for the normal component of $\boldsymbol{F}_r$.

Steady states results are presented in Fig. 6, where we display the patterns of the radiative energy for both the P_1 and M_1 models. In Figs. 7 and 8 we plot the values along $x = 0.5$ in order to compare with the reference solution.

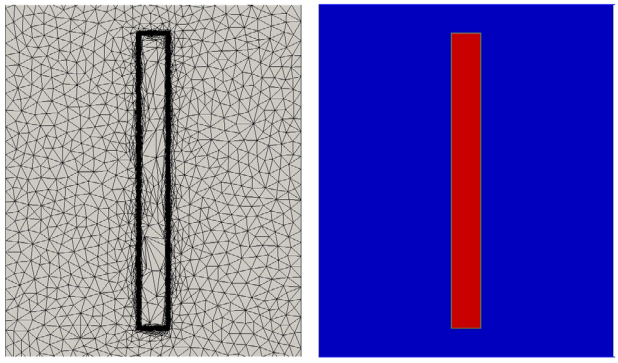

Fig. 5. Adapted mesh and the zero-level set of the signed distance function.

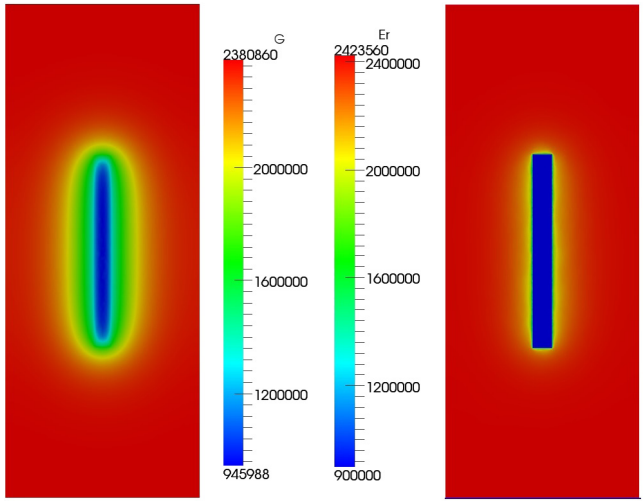

Fig. 6. Patterns of the radiative energy obtained for P_1 (left) and M_1 (right) models.

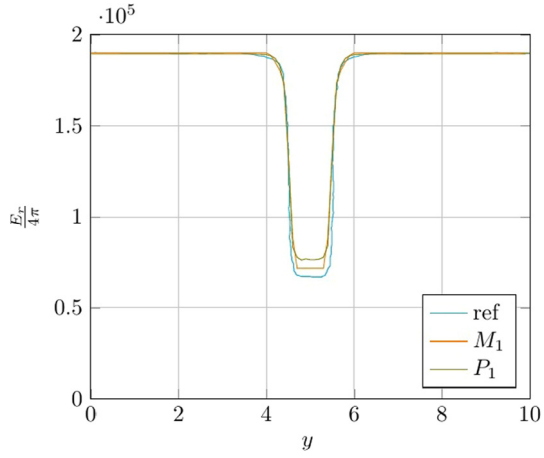

Fig. 7. Radiative energy along $x = 0.5$ compared to [56].

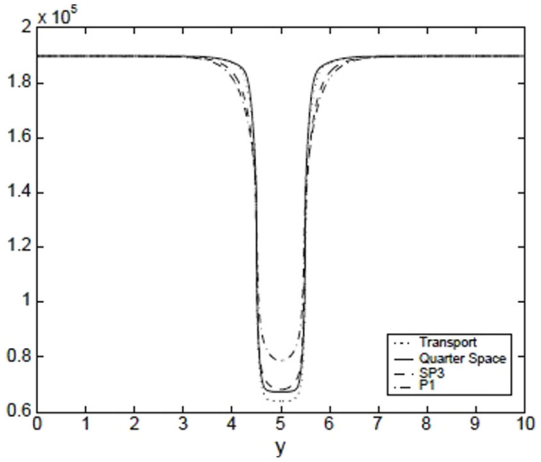

Fig. 8. Radiative energy along $x = 0.5$: from reference [56].

Table 1
Thermodynamical properties of the considered case.

Properties	Zone	
	Center zone	Outer zone
κ	100	0.05
σ	0	0,95
S_{rad}	0	1

As described in [56], the patterns show that both the P_1 and M_1 models overestimate the value of the radiative energy inside $\mathcal{D}_0$, but the solution obtained with the M_1 model is closer to the solution of the full radiative transfer equation than for the P_1 model. Again, this numerical test demonstrates that the obtained solution is stable and free of oscillations, justifying the coupled formulation and the stabilization developed here.

6.3. Radiation of an absorbing rod in a scattering media: the Mordant test

The next example to be presented was introduced in [58,59] and also presented in [37]. The considered domain is a unit square. The test represents a purely absorbing region (a square rod of side 0.6) surrounded by a scattering region. Only steady state results are presented. The properties of the different zones are summarized in Table 1. Again, the central zone and the heterogeneous properties are represented by means of the Immersed Volume Method. The problem setup, the adapted mesh (composed of 102 488 elements) and the level-set function used to adapt the mesh are presented in Fig. 9. In [37], results were compared with the results obtained by the discrete ordinates method, and it was shown that results from the M_1 model can differ for those obtained by classical discrete ordinates method due to complex geometrical effects. In this problem S_{rad} is a "manufactured" source term, as it is done in the quoted reference; this term is related to the Planckian distribution of the radiative intensity, but for this illustrative case, it was simply taken constant in each subdomain. The boundary conditions are zero Neumann on the left and bottom boundaries (i.e., weak boundary conditions), referred to as X_Γ in the following, and a specular reflection on the top and right boundaries, referred to as X_w in the following. For the M_1, for a boundary Γ, with $\boldsymbol{F}_r = (F_{rn}, F_{rt})$ being respectively the normal and tangential components of the flux, those conditions read:

$$
\begin{aligned}
E_{r,\Gamma} &= E_{r,w},\\
F_{rn,\Gamma} &= -F_{rn,w},\\
F_{rt,\Gamma} &= F_{rt,w},
\end{aligned}
$$

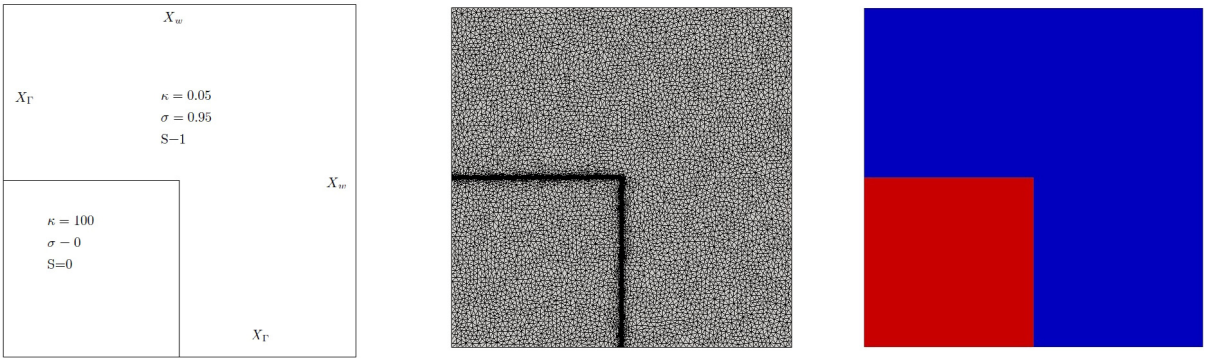

Fig. 9. Location of different boundary conditions (left), Adapted mesh (center) and the zero-level set of the signed distance function (right).

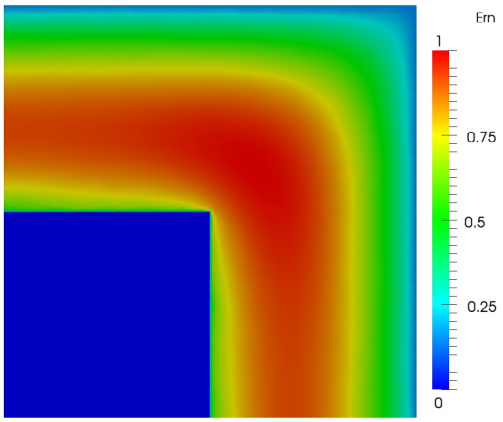

Fig. 10. Patterns obtained for M_1 model.

where X_Γ refers to quantities imposed on the considered boundary, and X_w are those obtained from the calculations (hence, those boundary conditions are updated at each time step). It is not straightforward to derive that kind of boundary conditions, since in the P_1 model the flux is related to the gradient of E_r , and therefore imposing E_r and ∇E_r on the same boundary would lead to an ill-posed problem. However, we tried the two alternatives, which give similar results; these results are presented below (see Figs. 10–13).

The M_1 results obtained, and in particular the behavior of the radiative energy close to the corner, are in good agreement with those obtained in [37]. Since a flux limited diffusion was used in that reference, the pattern obtained differs a bit, but the same tendency is observed.

6.4. Radiative transfer behind an obstacle: the shadow test

The purpose of this test, inspired in the benchmark presented in [60] and [61], is to show the ability of the M_1 model to capture the anisotropy of the radiative field, contrary to the P_1 model. All cited references computed results on half of the computational domain for symmetry reasons, but we have chosen to compute the whole domain. The geometry represents a cylindrical domain of 1.0 m in length and 0.12 m in radius. An ellipsoidal obstacle, of semi-major and semi-minor axes $(0.1, 0.06)$, respectively, is located in the domain. We have chosen values of absorption coefficient with a large difference between the obstacle and the surrounding media to produce a shadow effect ($\kappa_{\text{obstacle}} = 50\,000\ \text{m}^{-1}$, $\kappa_{\text{media}} = 0\ \text{m}^{-1}$). Contours of the obstacle are smoothed in [60], but this is replaced here by the anisotropic mesh adaptation to capture the interface of the obstacle properly. At the inlet (left boundary of the domain), a radiative energy of $E_{r,in} = 6.5\,10^6$ is imposed (strongly) and a zero Neumann (weak) boundary condition

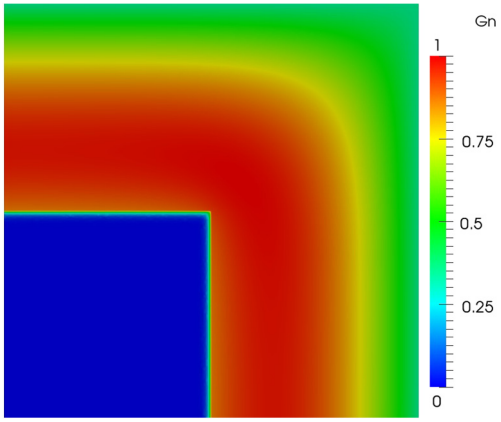

Fig. 11. Patterns obtained for P_1 model.

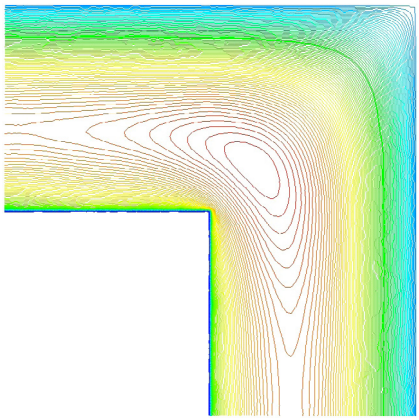

Fig. 12. Iso-lines obtained for M_1 model.

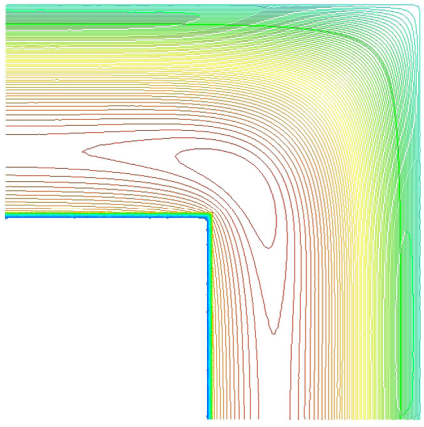

Fig. 13. Iso-lines obtained for P_1 model.

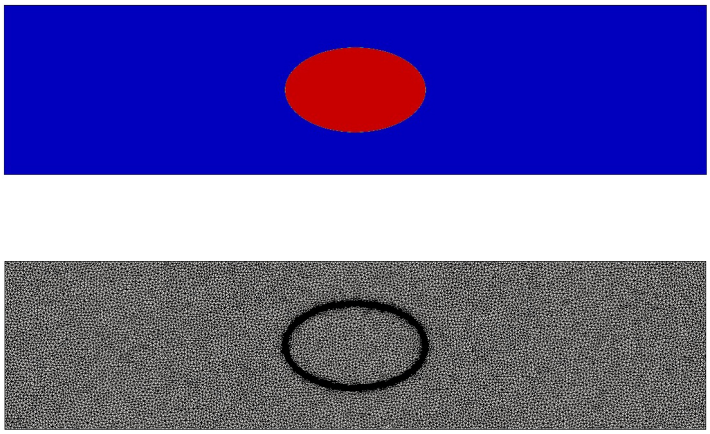

Fig. 14. Distributed absorption and adapted mesh.

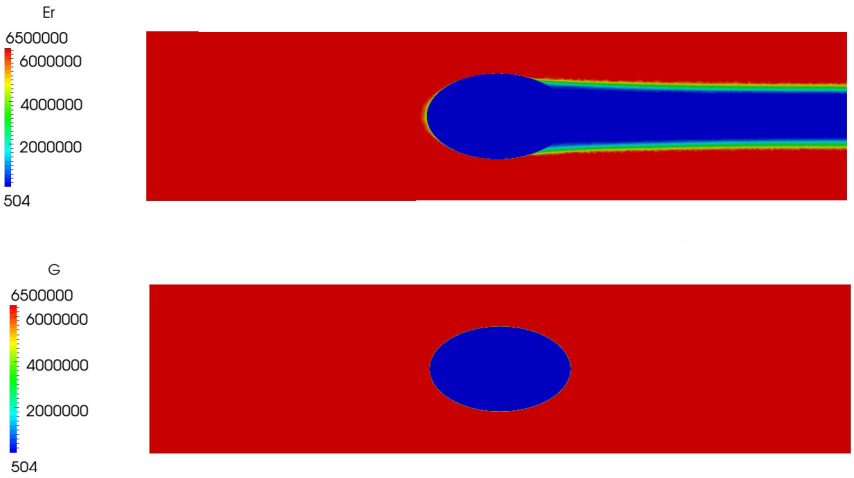

Fig. 15. Radiative energy for the P_1 model (bottom) and for the M_1 model (top).

is imposed for the normal component of the radiative flux $\boldsymbol{F}_r$ on the rest of the boundary. The initial condition is $E_r(\boldsymbol{x}, 0) = E_{r,0} = 5.04\ 10^2$. The distributed absorption coefficient and the mesh used for the computations are presented in Fig. 14. We only look for steady state results. A mesh of 268 012 elements is used.

As the obstacle is irradiated on one side by a distant source, the radiating source was fully illuminated almost instantaneously using the P_1 method. As expected, Fig. 15 shows that the M_1 model gives clearly a better approximation of the energy distribution. The shadow effect is in this case well represented highlighting the ability of the implemented method to reproduce and preserve strong angular variations in the radiation field. A small difference can be noticed when compared to results in [60] but this is mainly due to the high spatial resolution used and its discretization. Other properties for this test case can be investigated in future work by means of an asymptotic analysis, as shown in [62] or [63].

7. Concluding remarks

In this paper, a new stabilized finite element formulation for the M_1 radiation model has been developed and tested on some illustrative examples. The ability to represent multi-domain problems was also demonstrated. It is a first attempt to deal with such a coupled non-linear system that solves both radiative energy and flux. The interest of using a mixed formulation stabilized by the variational multiscale method is the fact that the approach is systematic,

in the sense that it provides a general framework for the structure of the stabilization terms on the one hand, and for the design the stabilization coefficients on the other hand. The resulting formulation does not require to use of mixed interpolations satisfying any inf–sup condition. However, the analysis of the accuracy of the formulation is difficult, since there exists only a few analytical solutions for the radiative transfer equation. These are usually given under an integral form, which makes it difficult to translate these solutions in terms of moments without using numerical integration. We recall that our purpose is to use the M_1 model for radiation in industrials furnaces, coupled with others physics (Navier–Stokes, heat balance, turbulence). Hence, the next step is the coupling with other equations and perform tests in 3D situations. Moreover, future work will consider further analysis on the proposed formulation showing that it preserves the admissible states: in a finite element context, this can be done by including the realizability constraints in the functional setting.

Acknowledgments

R. Codina acknowledges the support received from the ICREA Acadèmia Program, from the Catalan Government.

Appendix A. Calculation of the Jacobian matrixes

A.1. Calculation for the full Jacobians

Let δ_{ij} be the Kronecker delta associated to indexes i and j. Let also $\{\boldsymbol{e}_i\}_{1\leq i\leq d}$ be the canonical basis of $\mathbb{R}^d$. A third order tensor is denoted by $\underline{\underline{\mathbb{X}}}$, and its components are written as $(X^{ijk})_{1\leq i,j,k\leq d}$.

Let us recall the definitions

$$\mathbb{P}_r = \underbrace{\left(\frac{1-\chi}{2}\mathbb{I}_d + \frac{3\chi-1}{2}\frac{\boldsymbol{f}\otimes\boldsymbol{f}}{f^2}\right)}_{=\mathbb{D}(\boldsymbol{f})} E_r, \tag{A.1}$$

$$\chi(f) = \frac{3+4f^2}{5+2\sqrt{4-3f^2}}. \tag{A.2}$$

The Jacobian matrixes of $\mathbb{P}_r$ are defined by

$$\mathbb{J}_E = (\mathbb{J}_E^{ij})_{1\leq i,j\leq d} = \left(\frac{\partial \mathbb{P}_r^{ij}}{\partial E_r}\right)_{1\leq i,j\leq d} = \frac{\partial \mathbb{P}_r}{\partial E_r}, \tag{A.3}$$

$$\underline{\mathbb{J}_F} = (\underline{\mathbb{J}_F}^{ijk})_{1\leq i,j,k\leq d} = \left(\frac{\partial \mathbb{P}_r^{ij}}{\partial \boldsymbol{F}_r^k}\right)_{1\leq i,j,k\leq d} = \frac{\partial \mathbb{P}_r}{\partial \boldsymbol{F}_r}. \tag{A.4}$$

Using (A.1), one can write

$$\mathbb{J}_E = \mathbb{D} + E_r\frac{\partial \mathbb{D}}{\partial E_r}, \tag{A.5}$$

$$\underline{\mathbb{J}_F} = E_r\frac{\partial \mathbb{D}}{\partial \boldsymbol{F}_r}. \tag{A.6}$$

At this step, one can see that the tedious part of the calculation consists in differentiating $\chi(f)$ with respect to E_r and $\boldsymbol{F}_r$. We detail this calculation in the following.

We have that

$$\chi(f) = \chi\left(\left\|\frac{\boldsymbol{F}_r}{E_r}\right\|\right) \Rightarrow \begin{cases} \dfrac{\partial\chi}{\partial E_r} = \dfrac{\partial f}{\partial E_r}\dfrac{d\chi}{df} = -\dfrac{f}{E_r}\dfrac{d\chi}{df} \\ \dfrac{\partial\chi}{\partial \boldsymbol{F}_r} = \dfrac{\partial f}{\partial F_r^k}\dfrac{d\chi}{df} = \dfrac{F_r^k}{E_r\|\boldsymbol{F}_r\|}\dfrac{d\chi}{df}. \end{cases} \tag{A.7}$$

Moreover, one can easily show that

$$\frac{d\chi}{df} = \frac{2f}{\sqrt{4-3f^2}}. \tag{A.8}$$

Finally we have

$$\begin{cases} \dfrac{\partial \chi}{\partial E_r} = -\dfrac{2f^2}{E_r\sqrt{4-3f^2}} \\ \dfrac{\partial \chi}{\partial F_r^k} = \dfrac{F_r^k}{E_r\|\boldsymbol{F}_r\|}\dfrac{f}{\sqrt{4-3f^2}}. \end{cases} \tag{A.9}$$

Knowing this, the calculation of $\mathbb{J}_E$ is straightforward:

$$\frac{\partial \mathbb{D}}{\partial E_r} = \frac{1}{2}\frac{\partial \chi}{\partial E_r}\left(3\frac{\boldsymbol{F}_r \otimes \boldsymbol{F}_r}{\|\boldsymbol{F}_r\|^2} - \mathbb{I}_d\right). \tag{A.10}$$

Then we have

$$\boxed{\mathbb{J}_E = \mathbb{D} - \frac{f^2}{\sqrt{4-3f^2}}\left(3\frac{\boldsymbol{F}_r \otimes \boldsymbol{F}_r}{\|\boldsymbol{F}_r\|^2} - \mathbb{I}_d\right)}. \tag{A.11}$$

We now turn to $\frac{\partial \mathbb{D}}{\partial \boldsymbol{F}_r}$. We choose to make the differentiation component-wise. We can write

$$\mathbb{P}_r^{ij} = \frac{1-\chi}{2}\delta_{ij} + \frac{3\chi-1}{2}\frac{F_r^i F_r^j}{\|\boldsymbol{F}_r\|^2}. \tag{A.12}$$

We now have

$$\begin{aligned} \frac{\partial \mathbb{P}_r^{ij}}{\partial F_r^k} &= \frac{1}{2}\frac{\partial \chi}{\partial F_r^k}\left(3\frac{F_r^i F_r^j}{\|\boldsymbol{F}_r\|^2} - \delta_{ij}\right) + \frac{3\chi-1}{2}\left(\frac{\delta_{ik}F_r^k}{\|\boldsymbol{F}_r\|^2} + \frac{\delta_{kj}F_r^i}{\|\boldsymbol{F}_r\|^2} - \frac{2F_r^i F_r^j F_r^k}{\|\boldsymbol{F}_r\|^4}\right), \\ \frac{\partial \mathbb{P}_r^{ij}}{\partial F_r^k} &= \frac{f}{2E_r\sqrt{4-3f^2}}\left(3\frac{F_r^i F_r^j F_r^k}{\|\boldsymbol{F}_r\|^3} - \frac{\delta_{ij}F_r^k}{\|\boldsymbol{F}_r\|}\right) + \frac{3\chi-1}{2}\left(\frac{\delta_{ik}F_r^k}{\|\boldsymbol{F}_r\|^2} + \frac{\delta_{kj}F_r^i}{\|\boldsymbol{F}_r\|^2} - \frac{2F_r^i F_r^j F_r^k}{\|\boldsymbol{F}_r\|^4}\right). \end{aligned}$$

Re-arranging terms, we finally get

$$\boxed{J_F^{ijk} = \left(\frac{3f}{2E_r\sqrt{4-3f^2}} - \frac{3\chi-1}{\|\boldsymbol{F}_r\|}\right)\frac{F_r^i F_r^j F_r^k}{\|\boldsymbol{F}_r\|^3} + \frac{3\chi-1}{2}\left(\frac{F_r^j\delta_{ik}}{\|\boldsymbol{F}_r\|^2} + \frac{F_r^i\delta_{jk}}{\|\boldsymbol{F}_r\|^2}\right) - \frac{f}{2E_r\sqrt{4-3f^2}}\frac{F_r^k\delta_{ij}}{\|\boldsymbol{F}_r\cdot\|}}. \tag{A.13}$$

A.2. Calculation of the spectral radius

The expressions of the stabilization parameters (50) and (51) involve the spectral radii of $\mathbb{J}_E$ and $\mathbb{J}_F^k$, the second order tensor of components J_F^{ijk}. So we need to get an expression, or at least an approximation to these spectral radii. For $\mathbb{J}_E$, since we know that

$$\rho(\mathbb{D}) = \max\left(\chi, \frac{1-\chi}{2}\right),$$

it is necessary to calculate the spectral radius of

$$\mathbb{B} = 3\frac{\boldsymbol{F}_r \otimes \boldsymbol{F}_r}{\|\boldsymbol{F}_r\|^2} - \mathbb{I}_d.$$

Since $\boldsymbol{F}_r \otimes \boldsymbol{F}_r$ is a rank-one matrix and the trace of $\boldsymbol{F}_r \otimes \boldsymbol{F}_r$ is $\|\boldsymbol{F}_r\|^2$, we have

$$\rho\left(\frac{\boldsymbol{F}_r \otimes \boldsymbol{F}_r}{\|\boldsymbol{F}_r\|^2}\right) = 1 \;\Rightarrow \rho(\mathbb{B}) = 2.$$

From this we obtain

$$\boxed{\rho(\mathbb{J}_E) = \rho(\mathbb{D}) - \frac{2f^2}{\sqrt{4-3f^2}}}. \tag{A.14}$$

Using similar arguments about rank-one matrixes, one can obtain

$$\boxed{\rho(\mathbb{J}_F^k) = \frac{4\alpha|F_r^k|}{\|\boldsymbol{F}_r\|}}, \tag{A.15}$$

$$\boxed{\sum_{k=1}^{d} \rho(\mathbb{J}_F^k) = \frac{4\alpha\|\boldsymbol{F}_r\|_1}{\|\boldsymbol{F}_r\|_2}}, \tag{A.16}$$

with

$$\alpha = \frac{f}{2cE_r\sqrt{4-3f^2}}.$$

Appendix B. Algorithm for the proposed formulation

At this point, for sake of clarity, we will make the difference with "time" right hand side (coming from discretization of terms $\frac{\delta \boldsymbol{F}_{r,h}^{i+1}}{\delta t}$ and $\frac{\delta E_{r,h}^{i+1}}{\delta t}$) and "non linear" right hand sides (actual right hand sides of (30) and (31)). The superscripts are n and i, respectively. An algorithm for this formulation can be found in the table below:

Given $(\boldsymbol{F}_r^n, E_r^n)$;
at the first non-linear iteration ($i = 0$), set $\boldsymbol{F}_r^0 = \boldsymbol{F}_r^n$ and $E_r^0 = E_r^n$;
compute the local "time" right hand sides of (30) and (31) ;
assemble a global "time" right hand side ;
while $(\ \|E_r^{i+1} - E_r^i\| \leq \varepsilon_E \ AND \ \|\boldsymbol{F}_r^{i+1} - \boldsymbol{F}_r^i\| \leq \varepsilon_F\ )$ **do**
  compute $\boldsymbol{f}^i$;
  compute $\chi(\boldsymbol{f}^i)$ with (14) ;
  compute $\mathbb{D}(\boldsymbol{f}^i)$ with (13) ;
  compute $\mathbb{P}_r^i$, $\mathbb{J}_E^i$ and $\underline{\mathbb{J}_F^i}$ using (13),(A.11) and (A.13);
  compute elementary matrix and "non linear" right hand side corresponding to (30) and (31) ;
  assemble a global matrix and a global "non linear" right hand side ;
  compute the global "total" right-hand side (with "time" and "non linear" contributions);
  solve the system $\rightarrow (\boldsymbol{F}_r^{i+1}, E_r^{i+1})$;
  update $\boldsymbol{F}_r$ and E_r;
end
at last non linear iteration i_{end}, $\boldsymbol{F}_r^{n+1} = \boldsymbol{F}_r^{i_{end}}$ and $E_r^{n+1} = E_r^{i_{end}}$;

Algorithm 1: algorithm for M_1 finite element method described above

References

[1] J. Kang, Y. Rong, Modeling and simulation of load heating in heat treatment furnaces, J. Mater. Process. Technol. 174 (1) (2006) 109–114.
[2] E. Keramida, H. Liakos, M. Founti, A. Boudouvis, N. Markatos, Radiative heat transfer in natural gas-fired furnaces, Int. J. Heat Mass Transfer 43 (10) (2000) 1801–1809.
[3] A. Habibi, B. Merci, G.J. Heynderickx, Impact of radiation models in CFD simulations of steam cracking furnaces, Comput. Chem. Eng. 31 (11) (2007) 1389–1406.
[4] D. Cepite, A. Jakovičs, B. Halbedel, Modelling convective and radiative heat transfer in a glass melting model crucible, Magnetohydrodynamics (4) (2009) 587.
[5] F.-T. Lentes, N. Siedow, Three-dimensional radiative heat transfer in glass cooling processes, Glastech. Ber. Glass Sci. Technol. 72 (6) (1999) 188–196.
[6] H.T. Kim, B.W. Rhee, J.H. Park, Benchmark calculations of a radiation heat transfer for a CANDU fuel channel analysis using the CFD code, J. Nucl. Sci. Technol. 43 (11) (2006) 1422–1430.
[7] R. Viskanta, M. Mengüç, Radiation heat transfer in combustion systems, Prog. Energy Combust. Sci. 13 (2) (1987) 97–160.

[8] L. Tessé, F. Dupoirieux, J. Taine, Monte Carlo modeling of radiative transfer in a turbulent sooty flame, Int. J. Heat Mass Transfer 47 (3) (2004) 555–572.
[9] B. Garten, F. Hunger, D. Messig, B. Stelzner, D. Trimis, C. Hasse, Detailed radiation modeling of a partial-oxidation flame, Int. J. Therm. Sci. 87 (2015) 68–84.
[10] M. Frank, A. Klar, E. Larsen, S. Yasuda, Approximate models for radiative transfer, Bull. Inst. Math. Acad. Sin. 2 (2) (2007) 409.
[11] R.G. McClarren, C.D. Hauck, Robust and accurate filtered spherical harmonics expansions for radiative transfer, J. Comput. Phys. 229 (16) (2010) 5597–5614.
[12] K. Stamnes, S.-C. Tsay, K. Jayaweera, W. Wiscombe, et al., Numerically stable algorithm for discrete-ordinate-method radiative transfer in multiple scattering and emitting layered media, Appl. Opt. 27 (12) (1988) 2502–2509.
[13] W.W. Yuen, The multiple absorption coefficient zonal method (MACZM), an efficient computational approach for the analysis of radiative heat transfer in multidimensional inhomogeneous nongray media, Numer. Heat Transfer B 49 (2) (2006) 89–103.
[14] B. Dubroca, J.-L. Feugeas, Etude théorique et numérique d'une hiérarchie de modèles aux moments pour le transfert radiatif, C. R. Acad. Sci., Paris I 329 (10) (1999) 915–920.
[15] M. González, E. Audit, P. Huynh, HERACLES: a three-dimensional radiation hydrodynamics code, Astron. Astrophys. 464 (2) (2007) 429–435.
[16] M.A. Skinner, E.C. Ostriker, A Two-moment Radiation Hydrodynamics Module in Athena Using a Time-explicit Godunov Method, Astrophys. J. Suppl. Ser. 206 (2) (2013) 21.
[17] D. Aubert, R. Teyssier, A radiative transfer scheme for cosmological reionization based on a local Eddington tensor, Mon. Not. R. Astron. Soc. 387 (1) (2008) 295–307.
[18] D. Aubert, R. Teyssier, Reionization simulations powered by graphics processing units. I. On the structure of the ultraviolet radiation field, Astrophys. J. 724 (1) (2010) 244.
[19] M. Seaid, A. Klar, B. Dubroca, Flux limiters in the coupling of radiation and hydrodynamic models, J. Comput. Appl. Math. 168 (1) (2004) 425–435.
[20] B. Dubroca, M. Seaïd, I. Teleaga, A consistent approach for the coupling of radiation and hydrodynamics at low Mach number, J. Comput. Phys. 225 (1) (2007) 1039–1065.
[21] E. Hachem, T. Kloczko, H. Digonnet, T. Coupez, Stabilized finite element solution to handle complex heat and fluid flows in industrial furnaces using the immersed volume method, Internat. J. Numer. Methods Fluids 68 (1) (2012) 99–121.
[22] T. Coupez, Metric construction by length distribution tensor and edge based error for anisotropic adaptive meshing, J. Comput. Phys. 230 (7) (2011) 2391–2405.
[23] P.B. Bochev, M.D. Gunzburger, Least-squares Finite Element Methods, Vol. 166, Springer Science & Business Media, 2009.
[24] T.J. Hughes, G.R. Feijóo, L. Mazzei, J.-B. Quincy, The variational multiscale methoda paradigm for computational mechanics, Comput. Methods Appl. Mech. Engrg. 166 (1) (1998) 3–24.
[25] T.J. Hughes, Multiscale phenomena: Green's functions, the Dirichlet-to-Neumann formulation, subgrid scale models, bubbles and the origins of stabilized methods, Comput. Methods Appl. Mech. Engrg. 127 (1) (1995) 387–401.
[26] E. Hachem, B. Rivaux, T. Kloczko, H. Digonnet, T. Coupez, Stabilized finite element method for incompressible flows with high Reynolds number, J. Comput. Phys. 229 (23) (2010) 8643–8665.
[27] G. Scovazzi, Lagrangian shock hydrodynamics on tetrahedral meshes: A stable and accurate variational multiscale approach, J. Comput. Phys. 231 (24) (2012) 8029–8069.
[28] G. Scovazzi, B. Carnes, Weak boundary conditions for wave propagation problems in confined domains: Formulation and implementation using a variational multiscale method, Comput. Methods Appl. Mech. Engrg. 221 (2012) 117–131.
[29] A. Harten, P.D. Lax, B.V. Leer, On upstream differencing and Godunov-type schemes for hyperbolic conservation laws, SIAM Rev. 25 (1) (1983) 35–61.
[30] C. Berthon, P. Charrier, B. Dubroca, An HLLC scheme to solve The M 1 model of radiative transfer in two space dimensions, J. Sci. Comput. 31 (3) (2007) 347–389.
[31] C. Berthon, J. Dubois, B. Dubroca, T. Nguyen-Bui, R. Turpault, A free streaming contact preserving scheme for the M1 model, Adv. Appl. Math. Mech. 3 (2010) 259–285.
[32] K. Krycki, C. Berthon, M. Frank, R. Turpault, Asymptotic preserving numerical schemes for a non-classical radiation transport model for atmospheric clouds, Math. Methods Appl. Sci. 36 (16) (2013) 2101–2116.
[33] C. Buet, B. Despres, Asymptotic preserving and positive schemes for radiation hydrodynamics, J. Comput. Phys. 215 (2) (2006) 717–740.
[34] C. Buet, B. Després, E. Franck, An asymptotic preserving scheme with the maximum principle for the M1 model on distorded meshes, C. R. Math. 350 (11) (2012) 633–638.
[35] V. Vikas, C. Hauck, Z. Wang, R. Fox, Radiation transport modeling using extended quadrature method of moments, J. Comput. Phys. 246 (2013) 221–241.
[36] E. Olbrant, C.D. Hauck, M. Frank, A realizability-preserving discontinuous Galerkin method for the M1 model of radiative transfer, J. Comput. Phys. 231 (17) (2012) 5612–5639.
[37] M. González, C. García-Fernández, P. Velarde, 2D numerical comparison between Sn and M1 radiation transport methods, Ann. Nucl. Energy 36 (7) (2009) 886–895.
[38] H.-C. Zhou, D.-L. Chen, Q. Cheng, A new way to calculate radiative intensity and solve radiative transfer equation through using the Monte Carlo method, J. Quant. Spectrosc. Radiat. Transfer 83 (3) (2004) 459–481.
[39] C. Levermore, Relating Eddington factors to flux limiters, J. Quant. Spectrosc. Radiat. Transfer 31 (2) (1984) 149–160.
[40] G.N. Minerbo, Maximum entropy Eddington factors, J. Quant. Spectrosc. Radiat. Transfer 20 (6) (1978) 541–545.
[41] B. Dubroca, A. Klar, Half-moment closure for radiative transfer equations, J. Comput. Phys. 180 (2) (2002) 584–596.

[42] M. Frank, B. Dubroca, A. Klar, Partial moment entropy approximation to radiative heat transfer, J. Comput. Phys. 218 (1) (2006) 1–18.
[43] T. Coupez, E. Hachem, Solution of high-Reynolds incompressible flow with stabilized finite element and adaptative anisotropic meshing, Comput. Methods Appl. Mech. Engrg. 267 (1) (2013) 65–85.
[44] S. Badia, R. Codina, H. Espinoza, Stability, convergence and accuracy of stabilized finite element methods for the wave equation in mixed form, SIAM J. Numer. Anal. 52 (2014) 1729–1752.
[45] H. Espinoza, R. Codina, S. Badia, On some time marching schemes for the stabilized finite element approximation of the mixed wave equation, Comput. Methods Appl. Mech. Engrg. 296 (2015) 295–326.
[46] H. Espinoza, R. Codina, S. Badia, A Sommerfeld non-reflecting boundary condition for the wave equation in mixed form, Comput. Methods Appl. Mech. Engrg. 276 (2014) 122–148.
[47] R. Codina, Stabilized finite element approximation of transient incompressible flows using orthogonal subscales, Comput. Methods Appl. Mech. Engrg. 191 (39) (2002) 4295–4321.
[48] R. Codina, Finite element approximation of the hyperbolic wave equation in mixed form, Comput. Methods Appl. Mech. Engrg. 197 (13) (2008) 1305–1322.
[49] R. Codina, J. Principe, J. Baiges, Subscales on the element boundaries in the variational two-scale finite element method, Comput. Methods Appl. Mech. Engrg. 198 (2009) 838–852.
[50] R. Codina, J. González-Ondina, G. Díaz-Hernández, J. Principe, Finite element approximation of the modified Boussinesq equations using a stabilized formulation, Internat. J. Numer. Methods Fluids 57 (2008) 1305–1322.
[51] R. Codina, A stabilized finite element method for generalized stationary incompressible flows, Comput. Methods Appl. Mech. Engrg. 190 (20) (2001) 2681–2706.
[52] A.K. Pani, J.Y. Yuan, Mixed finite element method for a strongly damped wave equation, Numer. Methods Partial Differential Equations 17 (2) (2001) 105–119.
[53] T. Song, G. Scovazzi, A Nitsche method for wave propagation problems in time domain, Comput. Methods Appl. Mech. Engrg. 293 (2015) 481–521.
[54] O. Guasch, M. Arnela, R. Codina, H. Espinoza, A stabilized finite element method for the mixed wave equation in an ALE framework with application to diphthong production, Acta Acustica united with Acustica 102 (1) (2016) 94–106.
[55] S.C. Mishra, P. Talukdar, D. Trimis, F. Durst, Computational efficiency improvements of the radiative transfer problems with or without conduction—-a comparison of the collapsed dimension method and the discrete transfer method, Int. J. Heat Mass Transfer 46 (16) (2003) 3083–3095.
[56] M. Seaıd, M. Frank, A. Klar, R. Pinnau, G. Thömmes, Efficient numerical methods for radiation in gas turbines, J. Comput. Appl. Math. 170 (1) (2004) 217–239.
[57] E.W. Larsen, G. Thömmes, A. Klar, M. Seaıd, T. Götz, Simplified P_N approximations to the equations of radiative heat transfer and applications, J. Comput. Phys. 183 (2) (2002) 652–675.
[58] M. Mordant, Some efficient Lagrangian mesh finite elements encoded in ZEPHYR for two-dimensional transport calculations, Ann. Nucl. Energy 8 (11) (1981) 657–675.
[59] P.G. Dykema, R.I. Klein, J.I. Castor, A new scheme for multidimensional line transfer. III. A two-dimensional Lagrangian variable tensor method with discontinuous finite-element Sn transport, Astrophys. J. 457 (1996) 892.
[60] J.C. Hayes, M.L. Norman, Beyond flux-limited diffusion: parallel algorithms for multidimensional radiation hydrodynamics, Astrophys. J. Suppl. Ser. 147 (1) (2003) 197.
[61] M. Gonzalez, Contribution à l'étude Numérique de l'hydrodynamique Radiative: Des Expériences de Chocs Radiatifs Aux jets Astrophysiques (Ph.D. thesis), Université Paris Sud-Paris XI, 2006.
[62] C. Berthon, C. Chalons, R. Turpault, Asymptotic-preserving Godunov-type numerical schemes for hyperbolic systems with stiff and nonstiff relaxation terms, Numer. Methods Partial Differential Equations 29 (4) (2013) 1149–1172.
[63] C. Berthon, P. LeFloch, R. Turpault, Late-time/stiff-relaxation asymptotic-preserving approximations of hyperbolic equations, Math. Comp. 82 (282) (2013) 831–860.